Energy & Environmental Science

PAPER

Cite this: *Energy Environ. Sci.*, 2015, **8**, 3363

Defect-rich decorated TiO_2 nanowires for super-efficient photoelectrochemical water splitting driven by visible light†

Md Anisur Rahman, Samad Bazargan, Saurabh Srivastava, Xiongyao Wang, Marwa Abd-Ellah, Joseph P. Thomas, Nina F. Heinig, Debabrata Pradhan‡ and Kam Tong Leung*

Received 24th May 2015,
Accepted 21st September 2015

DOI: 10.1039/c5ee01615k

www.rsc.org/ees

Oxygen vacancy defects are highly desirable for photoelectrochemical water splitting reactions of TiO_2 nanomaterials because they act as electron donors and thereby enhance the electrical conductivity and charge transport property of TiO_2. For TiO_2 nanowires reported to date, oxygen vacancies are mainly generated by post-treatment of the as-synthesized nanowires. This comes with a disadvantage that oxygen vacancies are found to form just within a few tens of nanometers at the outer surface of these nanowires, and the photocurrent density is significantly reduced by two to three orders of magnitude when ultraviolet light is filtered out from the AM 1.5G light. Here, we demonstrate, for the first time, the controlled growth of 1D TiO_2 nanostructures with different morphologies and with incorporation of oxygen vacancy defects on a Si substrate by a single-step, catalyst-assisted pulsed laser deposition (PLD) method. Photoelectrochemical water splitting measurements under simulated sunlight show that the decorated nanowires exhibit one of the highest photoactivity values in the visible region (>430 nm) reported to date, which represents 87% of the overall photocurrent. The higher activity in the visible region can be attributed to more conductive TiO_2 nanostructures (*i.e.*, with a larger amount of oxygen vacancy defects), and the enhanced charge transfer from the nanocrystallites to the core of the decorated nanowires.

Broader context

Engineering the defects in wide band gap semiconducting transparent conductive oxide nanostructures is crucial in governing the physical and chemical properties of these structures. Compared to defect-free oxides, defect-rich oxides are more attractive for photovoltaics, photocatalysis, and fuel cell applications because of their narrower band gaps, which enable absorption of visible light, and a relatively high electrical conductivity. Enormous efforts have been made to narrow the band gap and extend the working spectrum to the visible light region, and these efforts include doping, defect creation by hydrogen treatment, and plasmonic nanoparticle sensitization. Unfortunately, all of these efforts provide two to three orders less photoactivity when ultraviolet light (<430 nm) is filtered out from the AM 1.5G spectrum. Moreover, synthesis of one-dimensional defect-rich TiO_2 nanostructures on conductive substrates by vapour deposition methods is extremely difficult due to the high melting temperature of TiO_2. The dependence of photoelectrochemical activity on the surface morphology of TiO_2 and the amount of oxygen vacancy defects in the 1D nanostructures is also not well understood. Despite recent developments, a simple method to fabricate defect-rich oxide semiconductors for efficient visible-light-driven photoactivity remains elusive. We have developed a simple one-step method using pulsed laser deposition to fabricate defect-rich 1D TiO_2 nanostructures, which show excellent photoelectrochemical activity under the visible light illumination.

Introduction

Over the past two decades, TiO_2 has been extensively studied as a photoanode for photoelectrochemical water splitting reaction due to its compatible band-edge positions, high photocatalytic activity, high resistance to photocorrosion, low cost, and lack of toxicity.[1] However, TiO_2 has a too wide band gap (3.0 eV)[2] to absorb sunlight in the visible region, which limits its photocatalytic activity to ultraviolet illumination. Several attempts

WATLab and Department of Chemistry, University of Waterloo, Waterloo, Ontario, N2L 3G1, Canada. E-mail: tong@uwaterloo.ca

† Electronic supplementary information (ESI) available: XRD patterns, XPS spectra of Ti 2p, UV-Vis reflectance spectra, Nyquist plots and the corresponding fitted results from the equivalent circuit model, gas quantification, and stability test. See DOI: 10.1039/c5ee01615k

‡ Present address: Materials Science Centre, Indian Institute of Technology Kharagpur, WB, 721302, India.

have been made to extend the light absorption of this catalyst, and they include doping,[3] hydrogen treatment,[4] and plasmonic nanoparticle sensitization.[5] All of these efforts have only managed to produce a photocurrent density not greater than 0.1 mA cm^{-2} in the visible region (>430 nm). The dependence of photoelectrochemical activity on the surface morphology and oxygen vacancies of these 1D TiO_2 nanostructures is also not well understood. As the surface morphology and electronic properties of TiO_2 nanostructures can affect the space charge regions differently, they are especially important for the overall charge collection efficiency by influencing the recombination velocity and the chemical reaction dynamics.[6] Furthermore, these nanostructures (such as nanobelts and nanowires) can also be used to enhance light harvesting and suppress charge carrier recombination while maintaining a high surface area necessary to improve the photoresponse.[7]

There are a variety of techniques to synthesize 1D TiO_2 nanostructures, including anodization of titanium foil or wires,[8] electrodeposition or solution precipitation,[9] hydrothermal methods,[10,11] thermal evaporation,[12–16] and chemical vapour deposition.[17] One major limitation of wet-chemistry methods is that the precursor materials are often incorporated into the final structure as impurities.[9,18] As a result, the charge transport efficiency and material stability are significantly reduced due to poor crystallinity, and grain boundaries. However, large-scale controlled synthesis of 1D TiO_2 nanostructures by vapour deposition is challenging due to the extremely low vapour pressures and high melting points of Ti and TiO_2. A protective buffer layer such as SiO_2, TiO_2 or TiN is often employed to activate the substrate-sensitive catalyst, including Ni,[13,19] Cu,[20] or Au,[17,21] in order to promote vapour–liquid–solid (VLS) growth of TiO_2 nanowires. In the absence of a buffer layer, the catalyst would quickly become poisoned, thus inhibiting VLS growth.[14] However, the presence of a dielectric or insulating buffer layer that is too thick on a conductive substrate has adverse effects on the growth characteristics[22] and charge collection efficiency,[23] which negatively impact the electronic properties of the nanodevices. A simple, alternative vapour deposition method to enable controlled synthesis of a 1D TiO_2 nanostructure on a conductive substrate with a buffer layer, of an appropriately optimized thickness (<50 nm), could therefore significantly advance future technological applications.

Unlike thermal evaporation and chemical vapour deposition, pulsed laser deposition (PLD) involves direct laser ablation of the target material, without affecting its stoichiometry, into the gaseous form, which is then exposed to the substrate held at a specified temperature. The absorption of a high-intensity laser energy pulse by a small volume of material leads to vaporization in the thermally non-equilibrium regime. As a result, activation of the gold catalyst could occur at a lower temperature, thus allowing the formation of 1D TiO_2 nanostructures at a lower temperature compared to other vapour deposition methods. Furthermore, variable substrate temperature, oxygen partial pressure and reductive growth environment during PLD can be used to control not only the rate of deposition but also the crystallinity, morphology and the amount of oxygen-related defects.[24] Oxygen vacancies are highly desirable for metal oxides because oxygen vacancy defects increase light absorption, act as electron donors and therefore enhance the electrical conductivity and charge transport property,[25] which can significantly improve their catalytic performance for photoelectrochemical water splitting reactions.[4]

Here, we use catalyst-assisted pulsed laser deposition (PLD) to synthesize defect-rich 1D TiO_2 nanostructures with a wide range of morphologies on a Si substrate by controlling a SiO_2 buffer layer of an appropriately optimized thickness and the growth temperature. We further demonstrate the remarkable photoelectrochemical catalytic performance of these defect-rich nanostructures for the first time in the visible light region (>430 nm) in a water splitting reaction.

Experimental

The catalyst-assisted PLD technique used to synthesize the 1D TiO_2 nanostructures has been described in detail elsewhere.[26] Briefly, the NanoPLD system (PVD Products) used in the present study was equipped with a KrF excimer laser (248 nm wavelength) and operated at a fluence of 350 mJ per pulse with a repetition rate of 5 Hz. The TiO_2 target was prepared by cold-pressing rutile TiO_2 powders (Aldrich, 99.99% purity) at a pressure of 25 MPa, followed by sintering in air at 900 °C for 12 h. The temperature of the substrate could be varied from room temperature to 900 °C by radiative heating from infrared heat lamps. The target-to-substrate distance was maintained at 25 mm with the substrate temperature kept at 675, 700, 720 or 750 °C to facilitate growth of nanostructures with different morphologies. Argon gas was let into the growth chamber at a constant flow rate of 19.8 sccm by using a mass flow controller to maintain a pressure of ~180 mTorr.

To evaluate the effect of the surface SiO_2 layer, we modified commercial p-type Si(100) chips (resistivity 0.001–0.002 ohm cm, Siegert Wafer) to produce three different substrates: (RCA-Si) chemically oxidized Si obtained after RCA cleaning; (H-Si) H-terminated Si obtained by etching with hydrofluoric acid; and (Ox-Si) thermally oxidized Si by annealing H-Si in O_2 at 850 °C for 120 min. Using a Filmetrics F-40 UV reflectometer, we estimated the respective oxide layer thicknesses for H-Si, RCA-Si and Ox-Si to be 1 nm, 3 nm and 30 nm. Gold nanoislands (GNIs) were produced on the three modified Si(100) substrates by magnetron sputtering a gold target for 4 s followed by annealing in N_2 at 500 °C for 30 min and the resulting templates were designated as GNI/RCA-Si, GNI/H-Si, and GNI/Ox-Si. The size distributions of the GNIs were measured by processing their SEM images using the ImageJ software.

The surface morphologies of the as-grown TiO_2 nanostructures on the three templates were characterized by field-emission scanning electron microscopy (SEM) using a Zeiss Merlin microscope. The crystal structures of the nanostructures were analyzed by glancing-incidence X-ray diffraction at an incidence angle of 0.3° using a PANalytical X'Pert Pro MRD diffractometer with Cu Kα radiation (1.54 Å). The transmission electron microscopy (TEM) study of the as-deposited structures was conducted using a Zeiss Libra 200 MC microscope. Reflectance spectra were

recorded using a Perkin-Elmer Lambda 950 UV-Vis-NIR spectrometer equipped with a Labsphere integrating sphere detector. The chemical-state compositions of the nanostructures were characterized by X-ray photoelectron spectroscopy (XPS) using a VG Scientific ESCALab 250 microprobe equipped with a monochromatic Al Kα X-ray source (1486.6 eV).

Photoelectrochemical measurements for the water splitting reaction using the TiO_2 nanostructures as the photocatalysts were carried out using an electrochemical station (CH Instruments, CHI 660E). We employed a standard three-electrode configuration, in which the TiO_2 nanostructures grown on the aforementioned templates, a saturated Ag/AgCl electrode, and a platinum wire were used as the working, reference, and counter electrodes, respectively, and a 1.0 M KOH solution was used as the electrolyte. A 300 W solar simulator (Newport-Oriel Instruments, Model 68811) was used to provide the AM 1.5G solar spectral illumination. The light intensity of the solar simulator was calibrated to 1 sun (100 mW cm^{-2}) using a power meter (Molectron, EPM 1000e). A short-pass (<400 nm) or a long-pass (>430 nm) filter (Oriel) was coupled with the AM 1.5G filter to isolate the UV or visible part of the simulated sunlight spectrum. Before each measurement, the electrolyte was thoroughly flushed with N_2 gas to remove any dissolved oxygen. The same electrochemical station was also used for the electrical impedance measurement by electrochemical impedance spectroscopy.

Results and discussions

Growth of defect-rich 1D nanostructures

The SEM images shown in Fig. 1 illustrate the effect of a SiO_2 buffer layer with different thicknesses on PLD growth of TiO_2 nanostructures at 700 °C. On a pristine H-Si substrate, laser ablation of the rutile TiO_2 target for 90 min produces nanobricks with an edge length of 150–250 nm and a thickness of 80–150 nm (Fig. 1a1). A similar film morphology is also observed on pristine RCA-Si (Fig. 1b1) and Ox-Si substrates (Fig. 1c1), which indicates that the presence of a SiO_2 layer, irrespective of its thickness, appears to have no significant effect on the TiO_2 film growth. In Fig. 1, we show that the mean diameters of the GNIs as-formed on the respective pristine substrates [4 ± 3 nm for H-Si (Fig. 1a2), 8 ± 3 nm for RCA-Si (Fig. 1b2), and 11 ± 3 nm for Ox-Si (Fig. 1c2)] increase with the increasing SiO_2 buffer layer thickness. The formation of much smaller GNIs on H-Si than RCA-Si and Ox-Si is due to the relative ease of Au silicide formation on the H-Si surface with the thinnest SiO_2 layer.[27] PLD growth of TiO_2 on the GNI/H-Si template for 90 min at 700 °C produces mainly flake-like nanostructures (Fig. 1a3), 300–400 nm long and 3–8 nm thick. The corresponding back-scattered electron images show that no GNI is present at the edges of these nanoflakes (Fig. 1a4). The presence of reactive Si dangling bonds at high temperature causes the Au atoms to bond strongly to the Si substrate,[27] and the resulting GNIs are therefore less prone to be lifted off. In contrast to the nanobrick film obtained on the pristine H-Si substrate (Fig. 1a1), the growth of nanoflakes on the GNI/H-Si template suggests that GNIs act as the nucleation sites and lower the surface energies of crystal growth planes, which consequently enhance the adsorption rate of gaseous species and promote the growth of flake-like nanostructures.[28] On the other hand, PLD growth on the GNI/RCA-Si template under the same deposition conditions produces TiO_2 nanowires that are notably different from flake-like nanostructures (Fig. 1b3 and b4). The surfaces of these straight nanowires appear to be smooth,

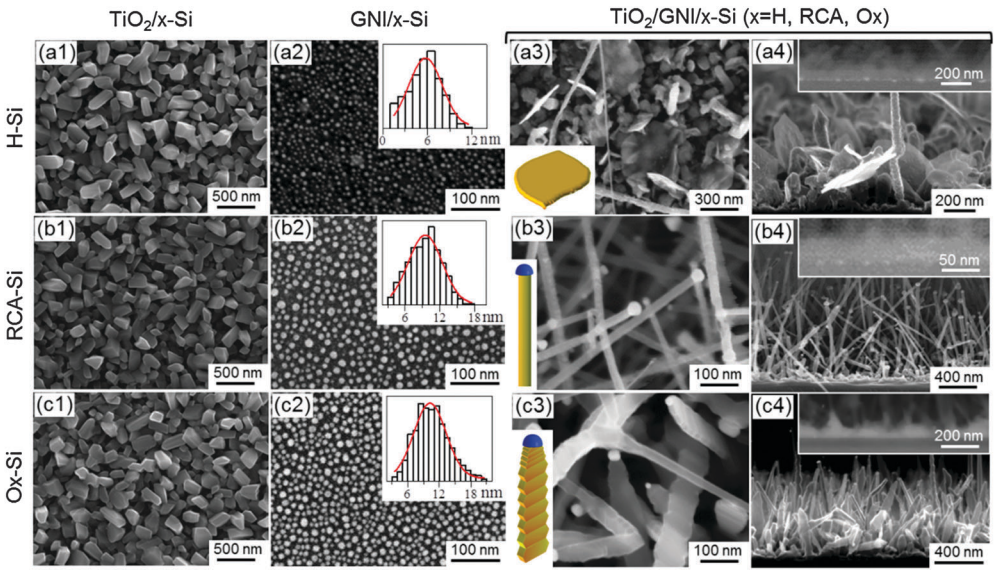

Fig. 1 SEM images of (a1, b1, and c1) typical TiO_2 nanobricks deposited in 200 mTorr Ar at 700 °C and (a2, b2, and c2) typical gold nanoislands (GNIs), with the corresponding near-Gaussian size distributions (insets), formed on H-Si (top row), RCA-Si (middle row) and Ox-Si (bottom row). SEM images of the TiO_2 nanostructures grown in 200 mTorr of Ar at 700 °C on GNI/H-Si (top row), GNI/RCA-Si (middle row), and GNI/Ox-Si templates (bottom row) taken as (a3, b3, and c3) top and (a4, b4, and c4) cross-sectional views. The insets in (a3, b3, and c3) schematically show the respective nanostructures. The insets in (a4, b4, and c4) show the corresponding cross-sectional backscattered electron images.

and each individual wire has a cross-sectional diameter of 10–15 nm along its entire length of several hundred nanometers. The length of the nanowires can be controlled by changing the deposition time. Evidently, the GNIs have been detached from the substrate and stay at the tips of individual nanowires, indicating a vapour–liquid–solid (VLS) growth mechanism for these nanowires.[29] However, the presence of a small amount of Au at the RCA-Si substrate interface (Fig. 1b4, inset), as in the case of GNI/H-Si (Fig. 1a4, inset), suggests that a fraction of Au has diffused through the interfacial SiO_2 layer at high temperature during the GNI formation and/or during TiO_2 deposition, producing Au–silicides at the interface. Interestingly, PLD growth on the GNI/Ox-Si template at 700 °C produces TiO_2 nanobelts, typically 10–20 nm thick, 50–80 nm wide and several hundred nm long (Fig. 1c3 and c4). The nanobelts have a pointy, triangular tip, with periodic sawtooth faceting along the sidewalls, the latter reflecting a remarkable oscillatory growth process.[30] Unlike the RCA-Si and H-Si templates, the thicker SiO_2 layer on the Ox-Si template prevents Au diffusion and the subsequent Au–silicide formation, as supported by the absence of Au at the interface (Fig. 1c4, inset).

We have also studied the effect of deposition (substrate) temperature on the nanostructure growth. Fig. 2 shows the SEM images of TiO_2 nanostructures grown on the three templates at 675 °C, 720 °C, and 750 °C, in addition to those obtained at 700 °C (already shown in Fig. 1a3, b3, and c3). Deposition at 675 °C produces, on all three templates, tapered corrugated nanowires with stacking faults distributed along the growth direction (Fig. 2a1, b1, and c1). Similar types of structures have also been reported for SiC[31] and ZnO nanowires.[32] On the other hand, deposition at 720 °C on GNI/H-Si produces pebble-like particles (Fig. 2a3), which is likely caused by complete consumption of the thin SiO_2 layer ($\sim$1 nm) *via* silicide formation.[33] As reported in earlier studies, annealing SiO_2 on Si under high vacuum conditions leads to decomposition of SiO_2 *via* the interfacial reaction: $Si + SiO_2 = 2SiO(g)$,[34,35] and the decomposition rate is further enhanced by the presence of Au.[36] The surfaces of these pebble-like particles are decorated with small nanoparticles. Interestingly, PLD growth at the same temperature (720 °C) on GNI/RCA-Si (Fig. 2b3) and GNI/Ox-Si templates (Fig. 2c3) leads to tapered nanowires also decorated with nanocrystallites on the surface, in marked contrast to the straight nanowires with smooth surfaces found on GNI/RCA-Si at 700 °C (Fig. 2b2). These decorated nanowires are found to be 0.8–1.5 μm long with an average diameter of 50–70 nm. A closer examination reveals that the nanocrystallites on these decorated nanowires are more concentrated at the base, and the surface of the decorated nanowires grown on GNI/Ox-Si (Fig. 2c3) appears to be rougher than that of the decorated nanowires on GNI/RCA-Si (Fig. 2b3). Deposition on the GNI/H-Si template at a higher temperature (750 °C) produces pebble-like structures (Fig. 2a4) similar to those obtained at 720 °C (Fig. 2a3). On GNI/RCA-Si, nanoflakes and pebble-like particles are observed at 750 °C (Fig. 2b4) and 770 °C (not shown), respectively, likely due to the gradual consumption of a thin SiO_2 layer (3 nm) *via* the interfacial reaction. In contrast to the GNI/H-Si (Fig. 2a4) and GNI/RCA-Si templates (Fig. 2b4), nanowires decorated with larger nanocrystallites grown on GNI/Ox-Si at 750 °C (Fig. 2c4) or higher temperatures are observed. In Fig. 3, we schematically summarize the different 1D TiO_2 nanostructures obtained on the three templates: GNI/RCA-Si, GNI/H-Si and GNI/Ox-Si, with the respective estimated thicknesses for the SiO_2 buffer layer of 1 nm, 3 nm, and 30 nm, at different growth temperatures.

Fig. 4 shows the corresponding transmission electron microscopy (TEM) images of representative TiO_2 nanostructures, including corrugated nanowires (Fig. 2b1), straight nanowires (Fig. 2b2), decorated nanowires (Fig. 2b3), and nanobelts (Fig. 2c2).

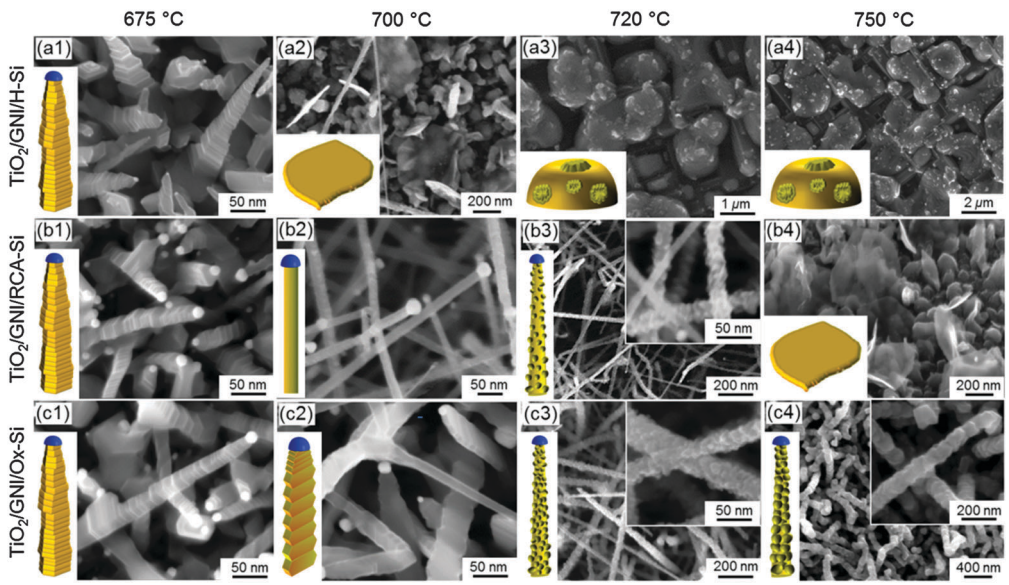

Fig. 2 SEM images of TiO_2 nanostructures grown in 20 mTorr Ar at (a1, b1, and c1) 675 °C, (a2, b2, and c2) 700 °C, (a3, b3, and c3) 720 °C, and (a4, b4, and c4) 750 °C on GNI/H-Si (top row), GNI/RCA-Si (middle row) and GNI/Ox-Si templates (bottom row). The corresponding lower left insets show schematic models of the respective as-grown nanostructures, with the magnified SEM images of selected nanostructures shown in the upper right insets.

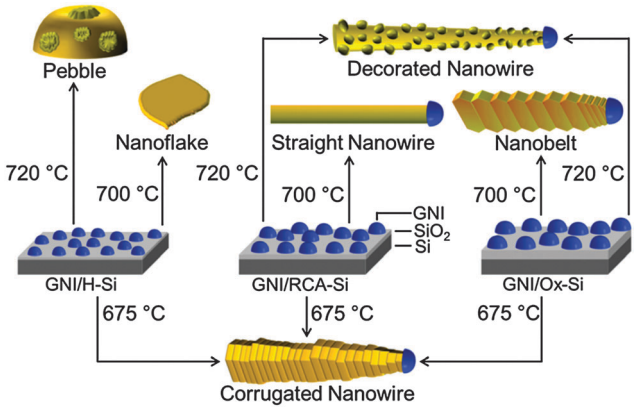

Fig. 3 Schematic models of TiO_2 nanostructures grown on gold nano-island (GNI) modified Si(100) templates at 675, 700 and 720 °C.

The rugged edges of the nanobelts (Fig. 4a) and corrugated nanowires (Fig. 4b) are clearly observed, while the surface of the straight nanowires appears to be smooth (Fig. 4c). For the decorated nanowires (Fig. 4d), the outer shell consists of nanocrystallites of 3–5 nm in size. The corresponding high-resolution TEM images (Fig. 4, insets) show that all the nanostructures are single-crystalline and have an interplanar spacing of 3.2 Å, corresponding to the (110) plane of bulk rutile TiO_2. Interestingly, the same rutile TiO_2 interplanar spacing is also found for individual nanocrystallites on the decorated nanowires (Fig. 4d, top inset). The corresponding lattice planes appear to be not perfectly aligned and disordered at the edges of the nanocrystallites (Fig. 4d, top inset), indicating the presence of

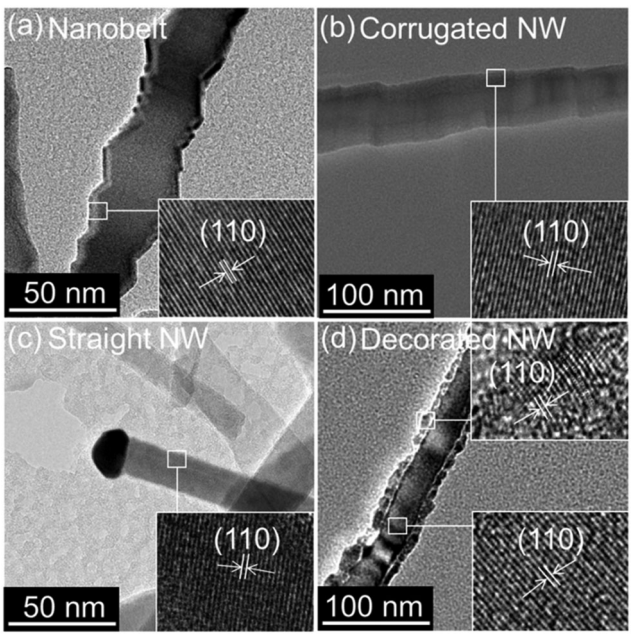

Fig. 4 TEM images of a typical (a) TiO_2 nanobelt, (b) corrugated nanowire (NW), (c) straight nanowire, and (d) decorated nanowire. The lower-right insets show the corresponding high-resolution TEM images, while the upper-right inset in (d) depicts the high-resolution TEM image of a nanocrystallite.

crystalline defects, including dislocations and local strains.[37] To further investigate the nature of crystallinity of the predominant nanostructures, we compare the glancing-incidence X-ray diffraction (XRD) patterns of the as-deposited nanostructures in Fig. S1 (ESI†). The prominent diffraction peaks are in good accord with the typical rutile structure of TiO_2 (PDF2 00-021-1276) and the FCC phase of metallic Au (PDF2 00-004-0784). Of particular interest is the remarkably different relative peak intensities of the prominent peaks at 27.4° (110), 36° (101) and 54.3° (211) with respect to the reference pattern of powder TiO_2 (PDF2 00-021-1276). Evidently, the higher intensity ratios of the (110) peak to (101) peak in all the nanowires and of the (110) peak to (211) peak in nanobelts than those in the reference pattern indicate that they have a preferred (110) growth orientation (in good accord with our TEM data).

As noted previously for other material systems,[38,39] the growth temperature can affect the catalyst state and, consequently, the predominant growth mode, *i.e.* vapour–solid growth below the eutectic temperature or VLS growth at or above the eutectic temperature, which ultimately governs the length and diameter of the nanowires. It has been observed that both vapour–solid and VLS growth can occur simultaneously, with the vapour–solid growth generally 10–100 times slower than VLS growth at the same precursor partial pressure and temperature.[39] In the present study, the growth temperature (675–750 °C) for the nanowires is lower than the lowest eutectic temperature in the bulk Au–Ti binary system (832 °C).[40] It should be noted that the actual eutectic temperature of a nanoscale material is expected to be lower than that of the bulk under the same pressure conditions.[41] We therefore expect that the growth of these nanowires occurs by both vapour–solid and VLS mechanisms as the catalyst state changes from a solid state to a liquid state throughout the temperature range. While both vapour–solid and VLS growth could occur concurrently, the VLS growth predominates at the higher growth temperature and the slower vapour–solid growth at a particular growth temperature could perturb and thus introduce variations into the general morphology of the nanowires. The formation of the tapered shape for the decorated nanowires has been attributed to the additional uncatalyzed vapour–solid growth occurring at the sidewalls, and to the longer exposure of the vapour to the base area compared to the tip area that ultimately affects the cross sectional shape of the nanowires.[42] The presence of a greater number of nanocrystallites on the decorated nanowires as-grown on GNI/Ox-Si than those on GNI/RCA-Si at a particular growth temperature suggests that the thicker, thermally grown SiO_2 layer (on Ox-Si) is rougher and has a different heat transfer efficiency than RCA-grown SiO_2, which ultimately affects the surface mobility, nucleation sites, and supersaturation rate of TiO_2, all of which control the morphology of the 1D nanostructures at a given temperature.[43] Our results also suggest that a minimum SiO_2 layer thickness of 3 nm (as formed on the RCA-Si substrate) is necessary for enabling VLS nanostructure growth in the PLD method, and a thicker SiO_2 or protective buffer layer is required for the growth of nanowires at a higher temperature. A buffer layer has been used in thermal evaporation and other methods for similar reasons,[44] but the

thickness of the buffer layer so employed has been considerably larger than 3–5 nm.[13,14] For example, TiO_x nanowires on Si were obtained by thermal evaporation (at 1100 °C) and a SiO_2 layer thickness of 65–120 nm was found to be necessary for efficient VLS growth.[14] In atmospheric pressure chemical vapor deposition, a 200 nm thick SiO_2 layer was coated with a 50 nm thick Ti layer for TiO_2 nanowire growth on Si(110) at 950 °C.[44] The SiO_2 buffer layer is used to modify the interaction between GNIs and the Si substrate for Au silicide formation and to provide a source of oxygen during growth in ambient Ar atmosphere. The thickness of the SiO_2 buffer layer therefore plays a critical role in the growth of TiO_2 nanowires on a Si substrate. The formation of different 1D nanostructures at different growth temperatures on GNI/RCA-Si (corrugated nanowires at 675 °C, straight nanowires at 700 °C, and decorated nanowires at 720 °C) and on GNI/Ox-Si (corrugated nanowires at 675 °C, nanobelts at 700 °C, and decorated nanowires at 720 °C or higher temperature) therefore confirms that both the growth temperature and the thickness of the SiO_2 buffer layer can be used complementarily to control the morphology of the 1D nanostructures.

In Fig. 5a, we show the changes in the colour of the as-deposited nanostructured films from blue (corrugated nanowires) to deep blue (straight nanowires) to greyish black (decorated nanowires), and then to lighter blue (nanobelts and nanobricks). It should be noted that the colours so observed for these nanostructured films remain unchanged for the respective films obtained by deposition for longer than 40 min. Moreover, the samples retain their individual colour upon storage in ambient atmosphere for over a year, indicating the robustness of these nanostructured films and that Ti^{3+} and/or oxygen vacancy defects are located in the bulk and not just at the surface of these nanostructures. Similar colour changes in TiO_2 due to difference in growth temperature and oxygen partial pressure as employed in the flame reduction method have also been reported.[45] Furthermore, hydrogen treatment has been used to create a high density of oxygen vacancies, which changed the colour of rutile TiO_2 from white to yellowish green and finally to black.[4] Recently, Ti^{3+}-related bulk defects in rutile TiO_2 have been found to exhibit five different colours, and the crystal colour appeared to correlate directly with the amount of defects.[46] Based on these studies and our experimental results, we hypothesize that the different colours for corrugated (light blue), straight (dark blue) and decorated nanowires (greyish black) are due to the differences in the amount of defects.

This series of colours should correlate with the respective degree of sub-stoichiometry of TiO_2 in these nanostructured films,[47] which is in good accord with our X-ray photoelectron data shown in Fig. 5b. For all the samples, the prominent Ti $2p_{3/2}$ peak at 459.4 eV corresponds to the Ti^{4+} state attributable to TiO_2, while the shoulder at 458.0 eV could be assigned to the Ti^{3+} state in TiO_x ($2 > x > 1$).[48,49] Four O 1s peaks at 530.7, 531.1, 532.6 and 533.3 eV correspond to TiO_2, TiO_x, SiO_2, and

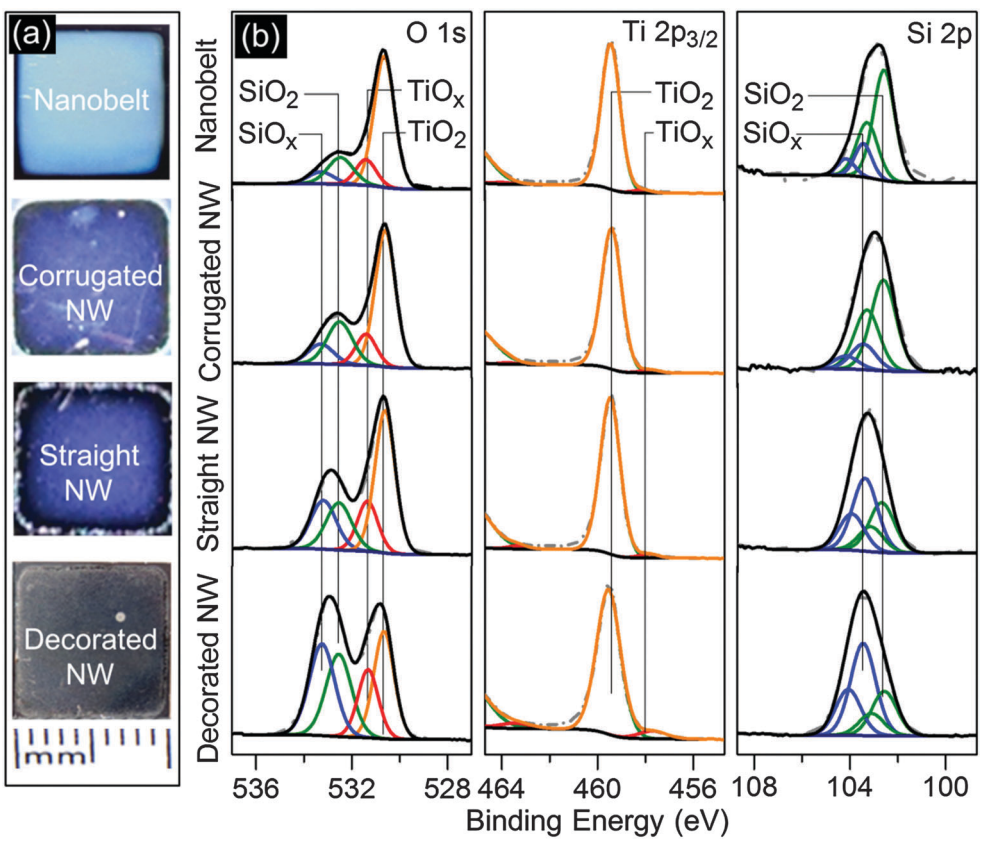

Fig. 5 (a) Photographs and (b) XPS spectra of O 1s, Ti $2p_{3/2}$, and Si 2p regions of TiO_2 nanostructured films consisting of nanobelts, corrugated nanowires (NWs), straight NWs, and decorated NWs.

SiO_x, respectively.[49,50] The fitted O 1s intensity ratios for TiO_x/TiO_2 and SiO_x/SiO_2 of the nanowires prepared on the GNI/RCA-Si template follow the order: decorated nanowires (720 °C) > straight nanowires (700 °C) > corrugated nanowires (675 °C), in close correlation with the growth temperature and sample colour (Fig. 5a). The Si $2p_{3/2}$ ($2p_{1/2}$) peaks at 102.6 (103.3) and 103.5 (103.2) eV correspond to SiO_2 and SiO_x, respectively.[50] For decorated nanowires, the Ti $2p_{3/2}$ peak width is found to be discernibly larger (Fig. S2, ESI†), which further supports the presence of a larger amount of oxygen vacancy defects in decorated nanowires than the other nanostructures.[51] The higher the growth temperature, the more reduced TiO_2 has become under the present synthesis conditions. On the other hand, the O 1s intensity ratio for TiO_x/TiO_2 of the nanobelts, deposited at the same temperature as that for straight nanowires on GNI/RCA-Si (700 °C) but on a GNI/Ox-Si template, is found to be smaller, which is consistent with the thicker SiO_2 layer on the GNI/Ox-Si template serving as a source of oxygen during growth in an Ar atmosphere. Less oxygen vacancy defects can therefore be expected in nanobelts than the nanowires grown on the GNI/RCA-Si template. As a result, the colour of the nanobelt film is lighter than the nanowire film (Fig. 5a). The corresponding reflectance spectra of the nanostructures all exhibit broadband absorption, starting at 330 nm and extending into the visible region of the spectrum (Fig. S3, ESI†). The intensity of the reflectance band increases with decreasing growth temperature for the nanowires, and with a larger interfacial SiO_2 layer thickness for the nanobelts, which is also consistent with the colour change of the samples. The visible light absorbance of the TiO_2 nanowires could be mainly attributed to the existence of defect states in the TiO_2 band gap,[22,52] likely due to the presence of Ti^{3+} defects and oxygen vacancies in accordance with the XPS analysis.

The slight deviation from perfect stoichiometry could result in a significant change in the electrical properties of the TiO_2 nanostructured films.[53] Fig. S4a (ESI†) shows the corresponding Nyquist plots for the nanostructured films under simulated sunlight illumination obtained by potentiostatic electrochemical impedance spectroscopy. Using the equivalent circuit model shown in Fig. S4b (ESI†), we determine the series resistance (R_S), the resistance (R_D) and chemical capacitance (CPE_D) of the semiconductor depletion layer in an RC circuit, along with the charge transfer resistance in the Helmholtz layer (R_H), the Warburg diffusion impedance (Z_W), and the capacitance of the electrochemical double layer (CPE_H) in a second RC circuit in series. The electrical parameters obtained by fitting the experimental data with the equivalent circuit are summarized in Table S1 (ESI†). The fitted data shows that the charge transfer resistances (R_S, R_D, and R_H) increase (while the capacitance decreases) in the following order: decorated nanowires < straight nanowires < corrugated nanowires < nanobelts, in close correlation with the observed oxygen vacancies and crystal colour. The higher charge transfer resistances of nanobelts might also be caused by the thicker interfacial SiO_2 layer, which ultimately reduces the collection efficiency of photogenerated electrons. Interestingly, the charge transfer resistance (R_D) at the depletion layer of decorated nanowires has become significantly smaller while the corresponding capacitance (CPE_D) has increased concomitantly, which suggests that the nanocrystallites of the decorated nanowires contain a large amount of oxygen vacancy defect states, likely in the band gap of the TiO_2 nanocrystallites. The sub-stoichiometric TiO_x ($2 > x > 1$) therefore possesses numerous advantages over stoichiometric TiO_2 because reduced TiO_x has higher absorbance, wettability,[54] and conductivity that are important for photoelectrochemical applications.

Photoelectrochemical properties

To study the photocatalytic activity of the aforementioned nanostructures for photoelectrochemical water splitting reaction, we employ, as photoanodes, TiO_2 nanobricks (grown on a pristine RCA-Si substrate, Fig. 1b1), corrugated nanowires (on a GNI/RCA-Si template, Fig. 2b1), straight nanowires (on a GNI/RCA-Si template, Fig. 2b2) and decorated nanowires (on a GNI/RCA-Si template, Fig. 2b3), as well as nanobelts (produced on a GNI/Ox-Si template, Fig. 2c2). The photocurrent spectra have been obtained over an illuminated sample area of 0.2 cm^2 under simulated sunlight illumination at 100 mW cm^{-2} using a 300 W xenon lamp coupled with an AM 1.5G filter. *In situ* quantification of the evolved gases by using an Universal Gas Analyser (Stanford Research Systems, SRS-UGA) confirms the stoichiometric splitting of water (Fig. S5, ESI†). The photocurrent density measured at 0.5 V (*vs.* Ag/AgCl) for the decorated nanowires (1.5 mA cm^{-2}) is found to be 8.3, 6.0, 2.5, and 1.6 times those of nanobelts (0.18 mA cm^{-2}), nanobricks (0.25 mA cm^{-2}), straight nanowires (0.6 mA cm^{-2}), and corrugated nanowires (0.94 mA cm^{-2}), respectively (Fig. 6a). We also characterize and obtain essentially no photocatalytic activity for the pristine RCA-Si substrate and GNI/RCA-Si template under the same conditions (Fig. 6a). The photogenerated holes in Si cannot be easily transferred to the valence band of TiO_2, likely due to a significant barrier at the junction resulting in carrier recombination in Si.[55] The higher photocurrent density observed for the decorated nanowires (and other nanostructures) can therefore be attributed only to the photogenerated charge carriers from the TiO_2 nanostructures themselves. The decorated nanowires provide one of the best photoelectrochemical performances among the TiO_2 nanostructures reported to date. The measured photocurrent density for the decorated nanowires (1.5 mA cm^{-2} at 0.5 V) in the present work is higher than those for most TiO_2 nanomaterials, including a modified rutile TiO_2 nanowire array obtained by depositing an epitaxial rutile TiO_2 shell onto a hydrothermally prepared rutile TiO_2 nanowire array (1.1 mA cm^{-2} at 0.5 V),[6] a hierarchical branched rutile TiO_2 nanorod array with the surface of the TiO_2 nanorod trunks covered by short needle-shaped TiO_2 branches (0.83 mA cm^{-2} at 0.7 V),[56] a N-modified rutile TiO_2 nanowire array with a cobalt cocatalyst (0.8 mA cm^{-2} at 0.7 V),[3] a TiO_2 nanoforest prepared by depositing dense TiO_2 nanorods along the entire TiO_2 nanotube trunk (0.75 mA cm^{-2}),[57] and an anatase TiO_2 nanotube array decorated with Ag nanoparticles (0.05 mA cm^{-2}).[58] Our current density is also comparable to that of flame-reduced TiO_2 nanowires (1.5 mA cm^{-2} at 0.58 V), where a complicated flame reduction method was used to control the oxygen vacancies

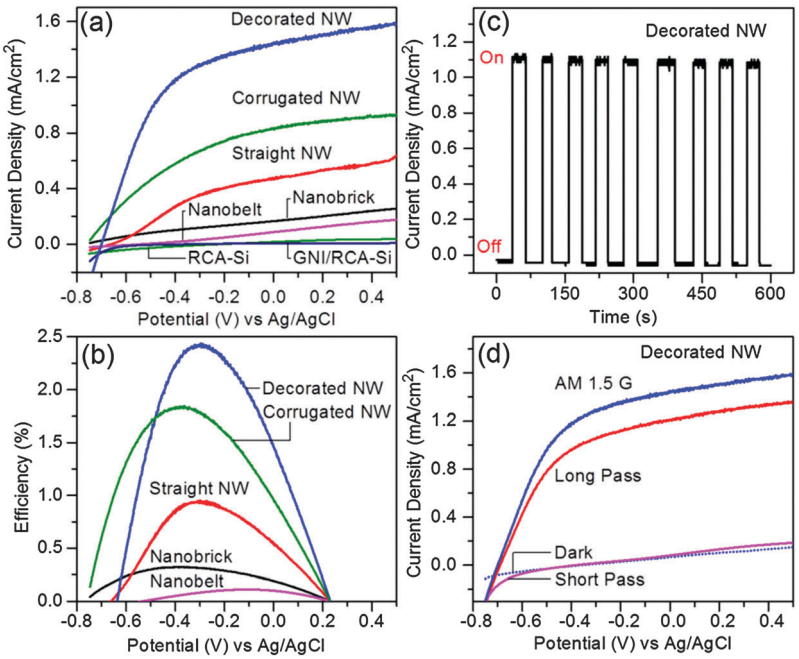

Fig. 6 (a) Current density and (b) the corresponding photoconversion efficiency measured as a function of the applied potential from different TiO_2 nanostructured photoanodes and from pristine RCA-Si, and RCA-Si/GNI templates (used as the control). The measurements are performed in a 1 M KOH solution at a scan rate of 10 mV s^{-1} under 100 mW cm^{-2} simulated sunlight illumination by a AM 1.5G filter. (c) Photocurrent density of decorated nanowires for repeated on/off cycles of simulated sunlight illumination. (d) Linear sweep voltammograms of the decorated TiO_2 nanowire photoanode from an AM 1.5G light (100 mW cm^{-2}) and with long-pass (>430 nm) and short-pass (<400 nm) filters.

by manipulating a minute variation of reduction time (a few seconds) or by adjusting a slight change in the fuel-to-air ratio.[59]

To quantitatively evaluate the efficiency of photoelectrochemical hydrogen generation from our TiO_2 nanostructures, the photoconversion efficiency is calculated by using the equation,[60]

$$\eta(\%) = j_p \frac{(1.23 - V)}{I_0} \times 100,$$

where j_p is the photocurrent density (in mA cm^{-2}) at the applied voltage V [*vs.* reversible hydrogen electrode (RHE)], and I_0 is the illumination intensity (*i.e.* 100 mW cm^{-2} for AM 1.5G).[3,4] A maximum photoconversion efficiency of 2.4% at −0.3 V *vs.* Ag/AgCl (or 0.7 V *vs.* RHE) is found for the decorated nanowires, followed by the corrugated nanowires (1.8% at −0.4 V *vs.* Ag/AgCl), straight nanowires (0.95% at −0.33 V *vs.* Ag/AgCl), nanobricks (0.32% at −0.44 V *vs.* Ag/AgCl), and nanobelts (0.11% at −0.09 V *vs.* Ag/AgCl), as shown in Fig. 6b. The lowest maximum photocurrent density found for the nanobelts can be attributed to the thicker SiO_2 buffer layer on the GNI/Ox-Si template, which impedes the photogenerated carrier transfer from the TiO_2 surface to the Pt counter electrode. The lower photocatalytic activity of the nanobricks on the RCA-Si template compared to nanowires is due to a shorter average length and a lower density of the as-grown nanobricks, and therefore a smaller specific surface area available for the water oxidation reaction. On the other hand, the higher photocatalytic activities of the decorated nanowires and corrugated nanowires compared to straight nanowires are attributed to the different morphologies of the nanowires. For the decorated nanowires, the shell consisting of densely packed ultrasmall nanocrystallites (3–5 nm) introduces a jagged surface at the nanowires. The "bumpy" surface evidently provides extra surface area for the photoelectrochemical reaction, while the junctions between the nanocrystallites act as additional active sites for oxygen production reaction.[61] Similarly, the rugged surface and nanojunctions in corrugated nanowires account for the observed higher catalytic activity than straight nanowires, but less than the decorated nanowires. Furthermore, to investigate the chemical and structural stabilities during photoelectrochemical water splitting, we perform chronoamperometric (current *vs.* time) studies with light on/off cycles at 100 mW cm^{-2} at 0 V *vs.* Ag/AgCl (or 1.0 V *vs.* RHE), the potential at which the photocurrent density has reached a plateau region (Fig. 6a). A typical measurement on the decorated nanowires shows a stable photocurrent density of 1.06 mA cm^{-2} with degradation of only 2.0% after 9 on/off cycles (Fig. 6c). (The corresponding Faradaic efficiency is estimated to be 95.1%.) The catalysts remain active even after six hours of photoelectrochemical water-splitting reaction (Fig. S6, ESI†). Similar stability tests have also been conducted on other nanostructures and they show virtually no degradation over repeated cycling and extended use.

Since TiO_2 is expected to be photoelectrochemically active mainly under UV light illumination due to its wide band gaps: 3.2 eV (388 nm) for anatase and 3.0 eV (410 nm) for rutile phases, and given that the AM 1.5G light contains only a small UV component, we determine the photocurrent densities arising from separate UV and visible spectral illuminations by coupling the AM 1.5G light with appropriate short-pass

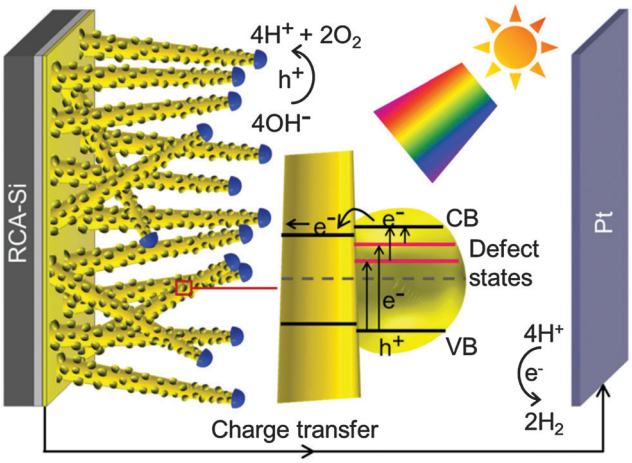

Fig. 7 Schematic diagram representing the charge separation and migration process in TiO_2 decorated nanowires in a photoelectrochemical water splitting reaction driven by visible light irradiation.

(<400 nm) and long-pass filters (>430 nm), respectively. As shown in Fig. 6d, the photocurrent density of decorated nanowires is reduced slightly from 1.5 mA cm^{-2} to 1.4 mA cm^{-2} when a long-pass filter is coupled with the AM 1.5G filter, and to effectively dark current density (0.18 mA cm^{-2}) when a short-pass filter is used. The photocurrent density observed for the decorated nanowire sample therefore mainly comes from the longer wavelength region (>430 nm), *i.e.*, the visible light region. This is a significant result, because unlike the previously reported case for rutile TiO_2 nanowire arrays decorated with Au nanoparticles,[5] where the observed photocurrent density (1.8 mA cm^{-2}) in AM 1.5G light was found to reduce by nearly 50% to 0.96 mA cm^{-2} with the UV light component (<430 nm) and to 0.00267 mA cm^{-2} with the visible light component (>430 nm), we observe only a 13% reduction with just the visible light component in the present work. Our visible light current density is also significantly higher than those reported for highly dense Si core TiO_2 shell nanowire arrays, obtained by depositing a polycrystalline anatase TiO_2 layer on a Si nanowire array, which gave zero photocurrent density under visible light.[55] Similarly, for H_2-treated[4] and Sn-doped TiO_2 nanowires,[62] almost zero photocurrent density was observed in visible light (>430 nm). These results verify that our decorated nanowire sample is the top photoelectrochemical catalysis performer in visible light (>430 nm) reported to date.

It has been reported that the band gap of TiO_2 and the amount of oxygen vacancy defects depend on the crystallite size. For example, when the crystallite size is decreased from 17 to 3 nm, the band gap is reported to increase from 3.2 to 3.6 eV and the deviation from stoichiometry (due to the presence of oxygen vacancies) has also increased with the increasing Ti^{3+} concentration.[45] Meanwhile, oxygen vacancies are found to introduce defect states below the conduction band of TiO_2.[22,52] The smaller (3–5 nm) rutile nanocrystallites on the decorated nanowires would therefore have a larger band gap than the single-crystalline nanowire host but possess defect states close to the conduction band minimum. A schematic band alignment diagram representing the enhancement mechanism of photoelectrochemical properties of decorated nanowires is shown in Fig. 7. When the decorated nanowires are irradiated with AM 1.5G light, electron transfer takes place from both valence band (VB) and oxygen vacancy defect states to the conduction band (CB) of TiO_2 nanocrystallites. The photon-excited electrons in the nanocrystallites are then injected into the conduction band of the core nanowires, while the photogenerated holes of nanocrystallites react with the donor species of the electrolyte. Owing to the single-crystalline nature of the nanowire core, the electrons in the conduction band of the nanowires could migrate easily to the Si substrate and ultimately to the counter electrode. The higher photocurrent density obtained from the decorated TiO_2 nanowires can therefore be attributed to the dense mat of nanowires[63] with densely packed TiO_2 nanocrystallites at the outer surface. These nanocrystallites offer excellent light-trapping characteristics, a large contact area with the electrolyte, and a highly conductive pathway for charge carrier collection, while the presence of a large number of oxygen vacancy defects in these nanocrystallites provides superior photoelectrochemical performance in the visible region.

Conclusion

By tuning the interfacial SiO_2 layer thickness and growth temperature, we have synthesized a variety of 1D nanostructured TiO_2 films, including nanobelts, corrugated nanowires, straight nanowires, and decorated nanowires, by using the catalyst-assisted PLD method. The use of a high vacuum system and the precise control of growth temperature and Ar flow have enabled us to produce (oxygen vacancy) defect-rich TiO_2 nanostructured films. We further demonstrate that the amount of oxygen vacancy defects depends on the growth temperature, and the electrochemical impedance measurement confirms the lower charge transfer resistances at the depletion layer of the decorated nanowires. The photoelectrochemical measurement under simulated sunlight (100 mW cm^{-2}) shows that these decorated nanowires exhibit a low onset potential of 0.3 V (*vs.* RHE) and a total energy photoconversion efficiency of 2.4%. More importantly, the photocurrent density of defect-rich decorated nanowires is reduced only slightly from 1.6 mA cm^{-2} to 1.4 mA cm^{-2} when the ultraviolet light component (<430 nm) is filtered out. Unlike the previously reported cases for sub-10 nm rutile nanoparticles,[64] Fe_2TiO_5 coated TiO_2 nanotube arrays,[65] (W, C) co-doped TiO_2 nanowires,[66] and Au nanoparticle decorated TiO_2 nanowire arrays,[5] where the observed photocurrent densities in AM 1.5G light were found to reduce by over 50% with just visible light illumination, we observe only a 13% reduction for the decorated nanowires. These defect-rich decorated nanowires therefore have the best photoelectrochemical catalytic performance in the visible region reported to date and are expected have a significant impact on the design of super-efficient photoanodes for photoelectrochemical applications driven by visible light.

The present photocurrent density of TiO_2 nanowires can be further increased with a longer PLD deposition time. When the

deposition time for the decorated nanowires is increased from 90 minutes to 130 minutes, the current density increases from 1.6 to 2.2 mA cm^{-2} (*i.e.* by 32%). This performance is especially remarkable considering the fact that both the length and density of the nanowires are smaller than most of the high-performance TiO_2 nanowire samples reported in the literature.[4,62] While the latter samples exhibit a current density of 2–3 mA cm^{-2}, these nanowires also have a higher aerial density and an average length of 5–15 μm, the larger amount of which inherently provides more active sites for the photoelectrochemical reaction. Furthermore, the present nanowires are prepared with one distinct advantage, *i.e.*, no need for any post-synthesis modification or treatment, in marked contrast to most of the aforementioned TiO_2 nanowire samples, all of which required post-treatment (such as annealing in a reductive environment) or doping with secondary materials. In our case, the photocurrent density and hence the efficiency could easily be increased further by increasing the aerial density of the nanowires (*e.g.*, by increasing the GNI density) and/or the length of the nanowires (*e.g.*, by increasing the deposition time). An even higher efficiency can be achieved by controlling doping with a second material (*e.g.*, Sn, Zn, Fe, or Cu) in the TiO_2 target. Furthermore, fabricating hybrid and/or core–shell nanowires and synthesizing binary or tertiary nanowires could also enhance the photoelectrochemical efficiency and can be easily accomplished by switching the targets (using a multi-target holder) during the growth of the TiO_2 nanowires. The present approach of intentionally growing defect-rich TiO_2 nanostructures by the catalyst-assisted PLD method could be extended to other wide-band gap semiconductors, which could offer viable alternatives for TiO_2 in a variety of solar energy driven applications, including photoelectrochemical water splitting, photocatalysis, and solar cells.

Acknowledgements

This work was supported by the Natural Sciences and Engineering Research Council of Canada.

References

1 M. Ni, M. K. H. Leung, D. Y. C. Leung and K. Sumathy, *Renewable Sustainable Energy Rev.*, 2007, **11**, 401–425.
2 A. L. Linsebigler, G. Lu and J. T. Yates, *Chem. Rev.*, 1995, 735–758.
3 S. Hoang, S. Guo, N. T. Hahn, A. J. Bard and C. B. Mullins, *Nano Lett.*, 2012, **12**, 26–32.
4 G. Wang, H. Wang, Y. Ling, Y. Tang, X. Yang, R. C. Fitzmorris, C. Wang, J. Z. Zhang and Y. Li, *Nano Lett.*, 2011, **11**, 3026–3033.
5 Y. C. Pu, G. Wang, K. D. Chang, Y. Ling, Y. K. Lin, B. C. Fitzmorris, C. M. Liu, X. Lu, Y. Tong, J. Z. Zhang, Y. J. Hsu and Y. Li, *Nano Lett.*, 2013, **13**, 3817–3823.
6 Y. J. Hwang, C. Hahn, B. Liu and P. Yang, *ACS Nano*, 2012, **6**, 5060–5069.
7 J. Tian, Z. Zhao, A. Kumar, R. I. Boughton and H. Liu, *Chem. Soc. Rev.*, 2014, **43**, 6920–6937.
8 A. Ghicov and P. Schmuki, *Chem. Commun.*, 2009, 2791–2808.
9 Z. Luo, W. Yang, A. Peng, Y. Zeng and J. Yao, *Nanotechnology*, 2009, **20**, 345601.
10 A. Riss, M. J. Elser, J. Bernardi and O. Diwald, *J. Am. Chem. Soc.*, 2009, **131**, 6198–6206.
11 J. Wu, S. Lo, K. Song, B. K. Vijayan, W. Li, K. A. Gray and V. P. Dravid, *J. Mater. Res.*, 2011, **26**, 1646–1652.
12 Z. G. Shang, Z. Q. Liu, P. J. Shang and J. K. Shang, *J. Mater. Sci. Technol.*, 2012, **28**, 385–390.
13 A. C. Dupuis, L. Jodin and E. Rouvière, *Appl. Surf. Sci.*, 2006, **253**, 1227–1235.
14 M. Lau, L. Dai, K. Bosnick and S. Evoy, *Nanotechnology*, 2009, **20**, 025602.
15 J. Wu, H. C. Shih and W. Wu, *J. Vac. Sci. Technol., B*, 2005, **23**, 2122.
16 J. Wu, H. C. Shih and W. Wu, *Nanotechnology*, 2006, **17**, 105–109.
17 C. A. Chen, Y. M. Chen, A. Korotcov, Y. S. Huang, D. S. Tsai and K. K. Tiong, *Nanotechnology*, 2008, **19**, 075611.
18 Y. V Kolen'ko, K. A. Kovnir, A. I. Gavrilov, A. V Garshev, J. Frantti, O. I. Lebedev, B. R. Churagulov, G. Van Tendeloo and M. Yoshimura, *J. Phys. Chem. B*, 2006, **110**, 4030–4038.
19 S. S. Amin, A. W. Nicholls and T. T. Xu, *Nanotechnology*, 2007, **18**, 445609.
20 J. Park, Y. Ryu, H. Kim and C. Yu, *Nanotechnology*, 2009, **20**, 105608.
21 J. Shi and X. Wang, *Cryst. Growth Des.*, 2011, **11**, 949–954.
22 F. M. Hossain, G. E. Murch, L. Sheppard and J. Nowotny, *Defect Diffus. Forum*, 2006, **251–252**, 1–12.
23 M. Mahanti and D. Basak, *RSC Adv.*, 2014, **4**, 15466–15473.
24 J. N. Zeng, J. K. Low, Z. M. Ren, T. Liew and Y. F. Lu, *Appl. Surf. Sci.*, 2002, **198**, 362–367.
25 M. K. Nowotny, L. R. Sheppard, T. Bak and J. Nowotny, *J. Phys. Chem. C*, 2008, **112**, 5275–5300.
26 S. Bazargan and K. T. Leung, *J. Phys. Chem. C*, 2012, **116**, 5427–5434.
27 Y. Sohn, D. Pradhan, A. Radi and K. T. Leung, *Langmuir*, 2009, **25**, 9557–9563.
28 Z. R. Dai, Z. W. Pan and Z. L. Wang, *Adv. Funct. Mater.*, 2003, **13**, 9–24.
29 A. M. Morales and C. M. Lieber, *Science*, 1998, **279**, 208–211.
30 F. M. Ross, J. Tersoff and M. C. Reuter, *Phys. Rev. Lett.*, 2005, **95**, 146104.
31 J. Chen, Y. Pan and R. Wu, *Physica E*, 2010, **42**, 2335–2340.
32 A. M. Glushenkov, H. Zhang, J. Zou, G. Q. Lu and Y. Chen, *J. Cryst. Growth*, 2008, **310**, 3139–3143.
33 J. F. Chang, T. F. Young, Y. L. Yang, H. Y. Ueng and T. C. Chang, *Mater. Chem. Phys.*, 2004, **83**, 199–203.
34 N. Miyata, H. Watanabe and M. Ichikawa, *Phys. Rev. Lett.*, 2000, **84**, 1043–1046.
35 H. Watanabe, K. Fujita and M. Ichikawa, *Appl. Phys. Lett.*, 1997, **70**, 1095–1097.
36 M. Liehr, H. Dallaporta and J. E. Lewis, *Appl. Phys. Lett.*, 1988, **53**, 589–591.

37 X. Chen, L. Liu, Z. Liu, M. A. Marcus, W. C. Wang, N. A. Oyler, M. E. Grass, B. Mao, P. A. Glans, P. Y. Yu, J. Guo and S. S. Mao, *Sci. Rep.*, 2013, **3**, 1510.

38 S. V. Thombare, A. F. Marshall and P. C. McIntyre, *APL Mater.*, 2013, **1**, 061101.

39 S. Kodambaka, J. Tersoff, M. C. Reuter and F. M. Ross, *Science*, 2007, **316**, 729–732.

40 Y. Matsuki, T. Inamura, K. Wakashima and H. Hosoda, *Mater. Trans., JIM*, 2007, **48**, 385–389.

41 L. C. Campos, M. Tonezzer, A. S. Ferlauto, V. Grillo, R. Magalhães-Paniago, S. Oliveira, L. O. Ladeira and R. G. Lacerda, *Adv. Mater.*, 2008, **20**, 1499–1504.

42 R. S. Wagner and W. C. Ellis, *Appl. Phys. Lett.*, 1964, **4**, 89–90.

43 J. C. Lee, K. S. Park, T. G. Kim, H. J. Choi and Y. M. Sung, *Nanotechnology*, 2006, **17**, 4317–4321.

44 J. M. Baik, M. H. Kim, C. Larson, X. Chen, S. Guo, A. M. Wodtke and M. Moskovits, *Appl. Phys. Lett.*, 2008, **92**, 242111.

45 A. Teleki and S. E. Pratsinis, *Phys. Chem. Chem. Phys.*, 2009, **11**, 3742–3747.

46 M. Li, W. Hebenstreit, U. Diebold, A. M. Tyryshkin, M. K. Bowman, G. G. Dunham and M. A. Henderson, *J. Phys. Chem. B*, 2000, **104**, 4944–4950.

47 J. Su, X. Zou and J. S. Chen, *RSC Adv.*, 2014, **4**, 13979–13988.

48 S. Hashimoto and A. Tanaka, *Surf. Interface Anal.*, 2002, **34**, 262–265.

49 Y. Mizuno, F. K. King, Y. Yamauchi, T. Homma, A. Tanaka, Y. Takakuwa and T. Momose, *J. Vac. Sci. Technol., A*, 2002, **20**, 1716–1721.

50 M. Chiodi, E. Cavaliere, I. Kholmanov, M. de Simone, O. Sakho, C. Cepek and L. Gavioli, *J. Nanopart. Res.*, 2010, **12**, 2645–2653.

51 H. Choi and M. Kang, *Int. J. Hydrogen Energy*, 2007, **32**, 3841–3848.

52 G. Li, Z. Lian, X. Li, Y. Xu, W. Wang, D. Zhang, F. Tian and H. Li, *J. Mater. Chem. A*, 2014, 1–9.

53 M. Radecka, A. Trenczek-Zajac, K. Zakrzewska and M. Rekas, *J. Power Sources*, 2007, **173**, 816–821.

54 D. Kuscer, J. Kovač, M. Kosec and R. Andriesen, *J. Eur. Ceram. Soc.*, 2008, **28**, 577–584.

55 Y. J. Hwang, A. Boukai and P. Yang, *Nano Lett.*, 2009, **9**, 410–415.

56 I. S. Cho, Z. Chen, A. J. Forman, D. R. Kim, P. M. Rao, T. F. Jaramillo and X. Zheng, *Nano Lett.*, 2011, **11**, 4978–4984.

57 Y. Yu, X. Yin, A. Kvit and X. Wang, *Nano Lett.*, 2014, **14**, 2528–2535.

58 K. Chen, X. Feng, R. Hu, Y. Li, K. Xie, Y. Li and H. Gu, *J. Alloys Compd.*, 2013, **554**, 72–79.

59 I. S. Cho, M. Logar, C. H. Lee, L. Cai, F. B. Prinz and X. Zheng, *Nano Lett.*, 2014, **14**, 24–31.

60 M. G. Walter, E. L. Warren, J. R. McKone, S. W. Boettcher, Q. Mi, E. A. Santori and N. S. Lewis, *Chem. Rev.*, 2010, **110**, 6446–6473.

61 W. Fan, Q. Zhang and Y. Wang, *Phys. Chem. Chem. Phys.*, 2013, **15**, 2632–2649.

62 M. Xu, P. Da, H. Wu, D. Zhao and G. Zheng, *Nano Lett.*, 2012, **12**, 1503–1508.

63 S. Bazargan and K. T. Leung, *J. Chem. Phys.*, 2013, **104704**, 1–9.

64 L. Li, J. Yan, T. Wang, Z. J. Zhao, J. Zhang, J. Gong and N. Guan, *Nat. Commun.*, 2015, **6**, 5881.

65 Q. Liu, J. He, T. Yao, Z. Sun, W. Cheng, S. He, Y. Xie, Y. Peng, H. Cheng, Y. Sun, Y. Jiang, F. Hu, Z. Xie, W. Yan, Z. Pan, Z. Wu and S. Wei, *Nat. Commun.*, 2014, **5**, 5122.

66 I. S. Cho, C. H. Lee, Y. Feng, M. Logar, P. M. Rao, L. Cai, D. R. Kim, R. Sinclair and X. Zheng, *Nat. Commun.*, 2013, **4**, 1723.